ELSEVIER

Earth and Planetary Science Letters 191 (2001) 267–282

EPSL

www.elsevier.com/locate/epsl

Fluid flow through rough fractures in rocks I: high resolution aperture determinations

Evgeny Isakov, Steven R. Ogilvie *, Colin W. Taylor, Paul W.J. Glover

Department of Geology and Petroleum Geology, University of Aberdeen, Aberdeen AB24 3UE, Scotland, UK

Received 1 February 2001; accepted 28 June 2001

Abstract

Full characterisation of rough fracture surfaces and the resulting variable apertures is an important step in the drive towards an improved understanding of the factors which control fluid flow through rocks. A number of surface profiling techniques exist, such as needle or laser profiling. However, these techniques are difficult and time consuming to apply to the total area of a fracture because they involve measuring a large number of parallel profiles, which are then difficult to align accurately. Hence, although a single profile may have high resolution in the *z*-direction and the direction of the profile, the fracture surface has a much lower resolution due to alignment errors. We have developed and improved considerably a previously existing optical concept for obtaining the topography of a fracture surface where the information about surface heights is measured simultaneously. The method relies on the construction of high fidelity transparent models of the fracture surface, which are imaged while covered with dyed and undyed water. The resulting images are converted to topography by a simple calibration procedure that makes use of the Lambert–Beer law. This method utilises in-house OptiProf™ software, which provides considerably more control over the imaging process than previous attempts at optical profiling. We have applied the technique to a range of rock fractures and test pieces, and have found the technique to work reliably, with lateral resolutions of 15 μm, and a vertical resolution of 15 μm, although all these could be improved by increasing the pixel count and the bit-depth of the camera, respectively.

Keywords: fluid dynamics; fractures; rocks; image analysis; physical models

1. Introduction

The single and multiphase flow of fluids through fractures in rocks depends upon many parameters which include (i) the densities and viscosities of the fluids, (ii) the relative saturations and distributions of the fluids, (iii) capillary pressure, (iv) the interfacial tensions and wetting angles of the fluids, (v) the direction of gravity, (vi) the flow rate, (vii) the connectivity of the fractures, (viii) the aperture of the fractures, (ix) the roughness of the fracture surfaces, and (x) the scale at which the measurement is made. These factors are comprehensively covered in the literature [1–8].

The study of fluid flow in rocks is a difficult one, partly because of the large amount of param-

* Corresponding author. Tel.: +44-1224-273456; Fax: +44-1224-272785.
E-mail address: s.ogilvie@abdn.ac.uk (S.R. Ogilvie).

0012-821X/01/$ – see front matter
PII: S0012-821X(01)00424-1

eters involved, but also because fracture systems in rocks are difficult to access and characterise. However, the solution of this problem is important in a wide range of applications relevant to the maintenance and improvement of human life on the Earth's surface. For example, the role of fractures can either aid the production of hydrocarbons by acting as patent flow channels, or can act as barriers to fluid flow, compartmentalising hydrocarbon reservoirs and hence making it difficult to produce the oil in place. Fractures also have a role to play in the provision of safe and plentiful drinking water, and in the contamination of such resources by domestic and industrial wastes. It is also important to understand the flow of fluids through fractures when contemplating the design of long-term subsurface storage of nuclear waste, or in the development of geothermal resources.

One approach to this problem is the use of numerical simulations of fluid flow in the subsurface. To do this accurately we need to know the effects of each of the parameters outlined above. In particular, it is important to ensure that a model for fluid flow incorporates a realistic rough fracture surface. This is because fracture roughness has a very important influence upon the flow of fluids, occurs at wide range of scales, with the surfaces being commonly fractal or multi-fractal [9,10].

In order to incorporate realistic fracture roughness into models of fluid flow in rough fractures we must be able to (i) measure the roughness of a range of fracture surfaces in nature, (ii) analyse the characteristic features of the measured surfaces, and (iii) create synthetic fractures numerically that share these characteristic features. Only then can the synthetic fractures be used for modelling fluid flow using the local cubic law, solution of Reynolds equation or solution of Navier–Stokes equation [11,12].

Two-dimensional (2D) roughness profiles may be measured by mechanical or optical methods. Needle or mechanical profilometers [8,13] work by tracking a stylus across the rough surface with surface elevations measured on a grid at various spacings. The vertical resolution of this type of profilometer is 10 μm [8]. This technique can measure surface heights with a precision of ± 0.1 μm but only gives a good horizontal resolution (ca. 0.02 μm) in one direction on the fracture plane. The resolution in the other direction can be greater than 1000 μm. This is because the mechanical profiling measures single profiles, one at a time. Complete coverage of the surface is not possible at high resolution because (i) it takes too long, and (ii) there are problems aligning accurately the multiple profiles.

Optical methods include laser profilometry [14], digital photogrammetry [15], and shadow profilometry [16]. Laser profilometry uses a laser instead of a mechanical needle, and interferometry of the reflected light to measure the height of the surface. Counter-intuitively, perhaps the laser profilometer has a worse resolution than the needle/mechanical method. It also suffers the same profiling and alignment problems as the mechanical profilometer. Digital photogrammetry involves the matching of the corresponding points of a stereopair to extract height information. In the study of Jessel et al. [15] this technique was reported to have a vertical resolution of ± 0.1 μm. Shadow profilometers [16] generate a profile by casting a shadow of a straight edge onto a rough surface. The shadow forms a profile of the surface roughness. There is the possibility of excessive lighting from numerous sources interfering with the intended light source; this would be a problem because the angle of incident light must be known in order to properly correct for the exaggeration.

Recently, apertures have been determined using the spectrophotometric analysis (SA) of epoxy replicas of fracture surfaces [1,17–20]. This involves the creation of transparent polymer models of the fracture surfaces and digital optical imaging of them while covered with a layer of dyed and undyed fluid. Nuclear magnetic resonance (NMR) [1,2] and X-ray computerised tomography (CT) [21,22] have the advantage over this technique in that they allow fluid–rock interactions to be observed within actual rock, thus avoiding any uncertainty in replication fidelity. In fact, CT-scanning has better resolution than NMR; the resolution of the scanner used by Keller [22] is 270×270 μm. NMR and CT-scanning are, how-

ever, expensive techniques, and have a lower spatial resolution in aperture measurement than the SA technique (of one order of magnitude according to Detwiler et al. [17]). Furthermore, SA gives more detailed measurements of each fracture half, hence a more accurate imaging of fracture aperture, and is fast and inexpensive to set up. However, these attempts suffer from (i) basic hardware image capture devices and uneven illumination of the subject, (ii) technical difficulties encountered during image capture, (iii) uncalibrated fluids resulting in arbitrarily scaled relative surface height measurements and (iv) lack of robust analysis procedures [1,19,23,24].

This paper describes the development of an improved optical method, which provides a fuller and more formalised framework for measuring the surfaces and apertures of fractures than previous attempts at utilisation of the Lambert–Beer law. This involves (i) advances in high fidelity polymer model (HFPM) preparation, (ii) significant improvements in hardware image capture, lighting and in firmware image capture, (iii) robust methodologies for reliably calibrating the fluids used in the imaging process, and (iv) improved control over the imaging process by using in-house developed OptiProf™ software to correct for technical difficulties and calculate the final measured topography of the surface by calibrating the image produced to dye thickness. This is a fast and high resolution process, allowing high resolutions (20–200 μm) to be attained in the mean plane of the fracture surface using modern high resolution digital cameras, and vertical resolutions of 20 μm and 0.1 μm if images are taken with a bit-depth of eight bits and 16 bits respectively. A method for analysing measured surface or aperture data and new methods for the creation of synthetic fractures that are tuned to have the same characteristic features as the measured ones are presented in a companion paper [25].

2. Experimental procedures

2.1. HFPMs

The first step is the creation of transparent

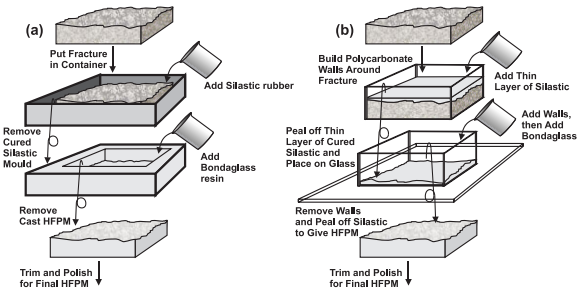

Fig. 1. The procedure for creating HFPMs. (a) The simple casting process. (b) The thin layer process.

HFPMs of the fracture surfaces. The fractured rock is initially trimmed to form a block with $120 \times 120 \times 100$ mm nominal dimensions. Two methods for the creation of HFPMs were used, and are shown in Fig. 1.

In the first method (Fig. 1a), each fracture half of the block was taken, cleaned with compressed air and placed in a deep tray, fracture face upwards. The tray was filled with Dow Corning Silastic® E RTV, which is a flexible mould-making rubber for intricate detail moulds that is supplied in two parts. When mixed together, the resulting mixture is of low viscosity, allowing the mixture to cover the rough surface of the rock completely. The mixture then cures to a white rubber with negligible shrinkage and exothermic heating, allowing the complex structure to be accurately reproduced without damage by thermal stresses. The rubbery nature of the final mould allows the original rock to be removed from the mould without damage to either surface. Occasionally, for friable rocks, it was found that the Silastic mould plucked mineral grains from the surface of the rock. This problem was also encountered by Yeo et al. [24]. It was found that this could be minimised by spraying the surface of the rock with an aerosol glue such as SprayMount®, a few minutes before moulding. The mould was cleaned with compressed air and filled with 400 cm^3 of Bondaglass® clear casting resin, which was allowed to set completely. It was found that bubbles or air could be trapped easily on the surface during this process, which was made worse by casting under a vacuum. However, washing the mould gently in warm water contain-

ing detergent removed the likelihood of bubbles occurring. When fully set, after 2 days, the casting resin was removed from the mould, trimmed to $100 \times 100 \times 30$ mm, and polished on all surfaces except that of the rough surface. It was found that the flexibility of the cured Silastic mould, while facilitating the removal of the original rock and the cast HFPM without damage, caused minor reproduction problems. Specifically, the weight of the casting resin distorted the centre of the mould resulting in a HFPM with a long wavelength artefact consisting of a slight mounding to the HFPM. While this was small, it had a significant effect upon the mating of the two halves of the HFPM. This artefact was removed by stiffening the mould by encapsulating within it stiff cardboard along its edges and base [1].

In the second method (Fig. 1b), each fracture half of the block was cleaned with compressed air and placed on a glass working surface. Thin polycarbonate walls were added to the sides of the sample secured using SprayMount®, which enabled easy removal of the sides. A thin layer, 5–10 mm thick, of Silastic® E RTV was poured over the surface, and left to cure. Again, SprayMount® mounting medium was used with friable rocks. The walls were removed, and the cured Silastic was pealed off carefully. The Silastic peal was then laid, rough surface uppermost, on a polished glass surface and surrounded by the walls once more. The walls were sealed to the glass using a smear of Vaseline®. The Bondaglass® clear casting resin was poured in on top of the Silastic peal and allowed to set as before. Once the casting resin had set, the walls were removed, and the Silastic layer was pealed off the cast model. The cast HFPM was then trimmed and polished as before. This second method uses much less Silastic and does not suffer from long wavelength artefacts because of the relatively thin layer of Silastic used, and the support given to it by the glass working surface. This method uses a similar amount of rubber as that of Yeo et al. [24], however, they produce perfectly mated surfaces from

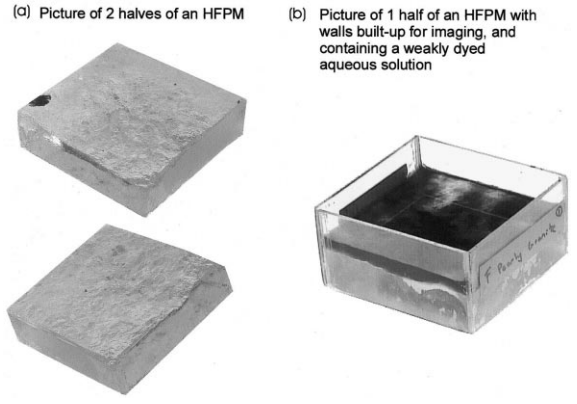

Fig. 2. Photographs of example HFPMs. (a) Two prepared HFPMs. (b) One HFPM arranged with walls to allow its topography to be measured as described in the text.

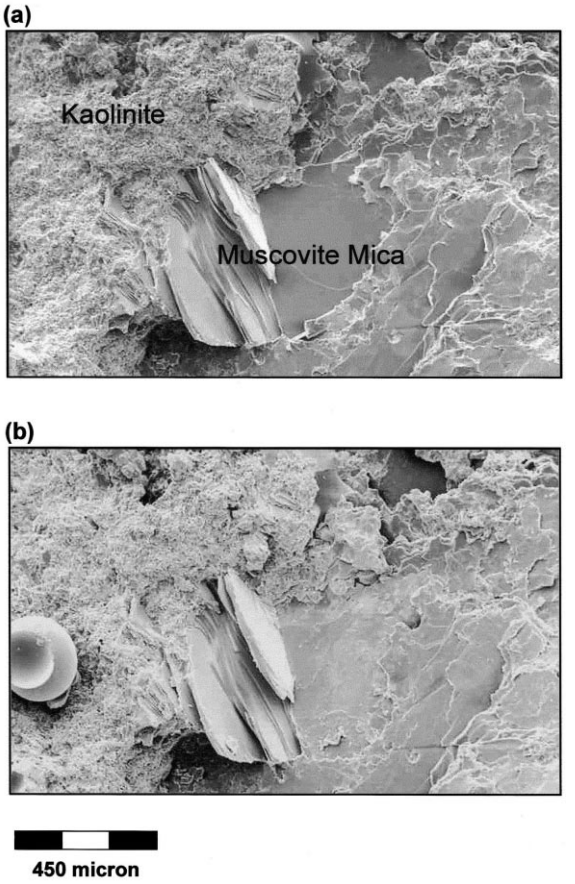

Fig. 3. The quality of reproduction of the surfaces by HFPMs. (a) SEM backscattered image of the surface of the original rock showing muscovite mica growth in two directions to the right of the field of view and kaolinite to the left, and (b) the exactly corresponding area of the resulting HFPM.

a single fracture surface rather than from both surfaces.

Two HFPM halves are shown in Fig. 2a. The quality of the reproduction of the HFPM was assessed by mounting a 5×5 cm block of the original rock fracture surface and its HFPM onto aluminium stubs, coated with gold, and imaging matching locations under a scanning electron microscope using secondary electron mode (SEI-SEM). Fig. 3 shows typical results from this test, which indicates that the fracture surface is reproduced typically to a resolution of better than 1 μm. This can be judged from Fig. 3, where the distance between the plates of muscovite mica is approximately 0.8 μm. The fidelity of reproduction is sufficiently high that only the presence of a gas bubble in the HFPM image allows the two images to be distinguished.

2.2. Digital optical imaging

Each of the HFPMs was subjected to digital optical imaging. Thin polycarbonate walls were attached to the sides of each HFPM. The resulting arrangement (Fig. 2b) was placed on a light box under a colour digital camera (640×480 pixels, eight-bit greyscale depth), which was attached to a PC equipped with a video capture board, as shown in Fig. 4. Note that this camera is relatively low resolution compared to many that are currently available. Its use in this paper gives a lateral resolution of 20 and 200 μm for imaged areas of 10×10 mm and 100×100 mm, respectively, and a vertical resolution of about 20 μm. This set-up is arranged so that the intensity of light captured by the camera can be accurately measured. Hence, the camera was set to manual exposure control, manual light colour balance, and a high quality manual aperture and focus zoom lens was used. In addition, the whole arrangement was shielded from ambient and reflected light, using black-out curtains and a thick rubber mat that covered all parts of the light box except that directly under the subject. The light source has a flicker frequency of 100 Hz. A number of technical difficulties were encountered in obtaining high quality images, these and their solutions are discussed in detail later in this paper.

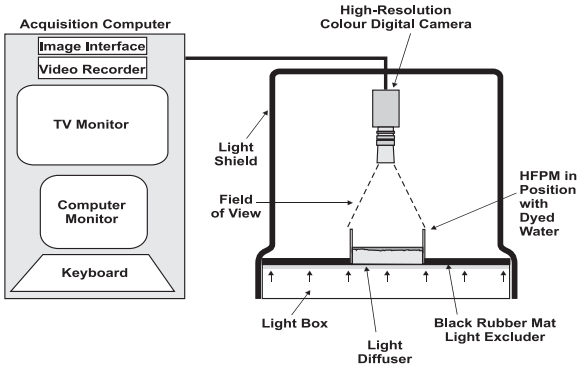

Fig. 4. The digital optical imaging set-up.

The principle of the technique is as follows. The HFPM is placed under the camera and imaged 20 times, first containing distilled water, and then containing the same amount of dyed water. These images represent the extent to which the incident intensity of light is absorbed by the presence of the HFPM and the fluid covering the surface. The ratio of the intensity of light for a given pixel at a given location on the fracture between the images containing dye and those containing water is related to the thickness of fluid covering the rough surface. This is described by the Lambert–Beer law. The calculation of the fluid thickness from the measured intensity ratio requires either (i) knowledge of the light extinction properties of the dye, whence the Lambert–Beer law can be used directly [1], or (ii) experimental calibration of dyed and undyed fluids, which, conversely, provides a measurement of the light extinction properties of the dye [19,20]. We opted for the latter approach. Finally, as the fluid surface is constrained to be horizontal by gravity, we can calculate the topography of the surface for each pixel (640×480) from the calibrated fluid thicknesses.

2.3. Lambert–Beer law

The Lambert–Beer law is described by the equation:

$$I_x = I_o e^{-KcT} \quad (1)$$

where I_x is the intensity of the transmitted light,

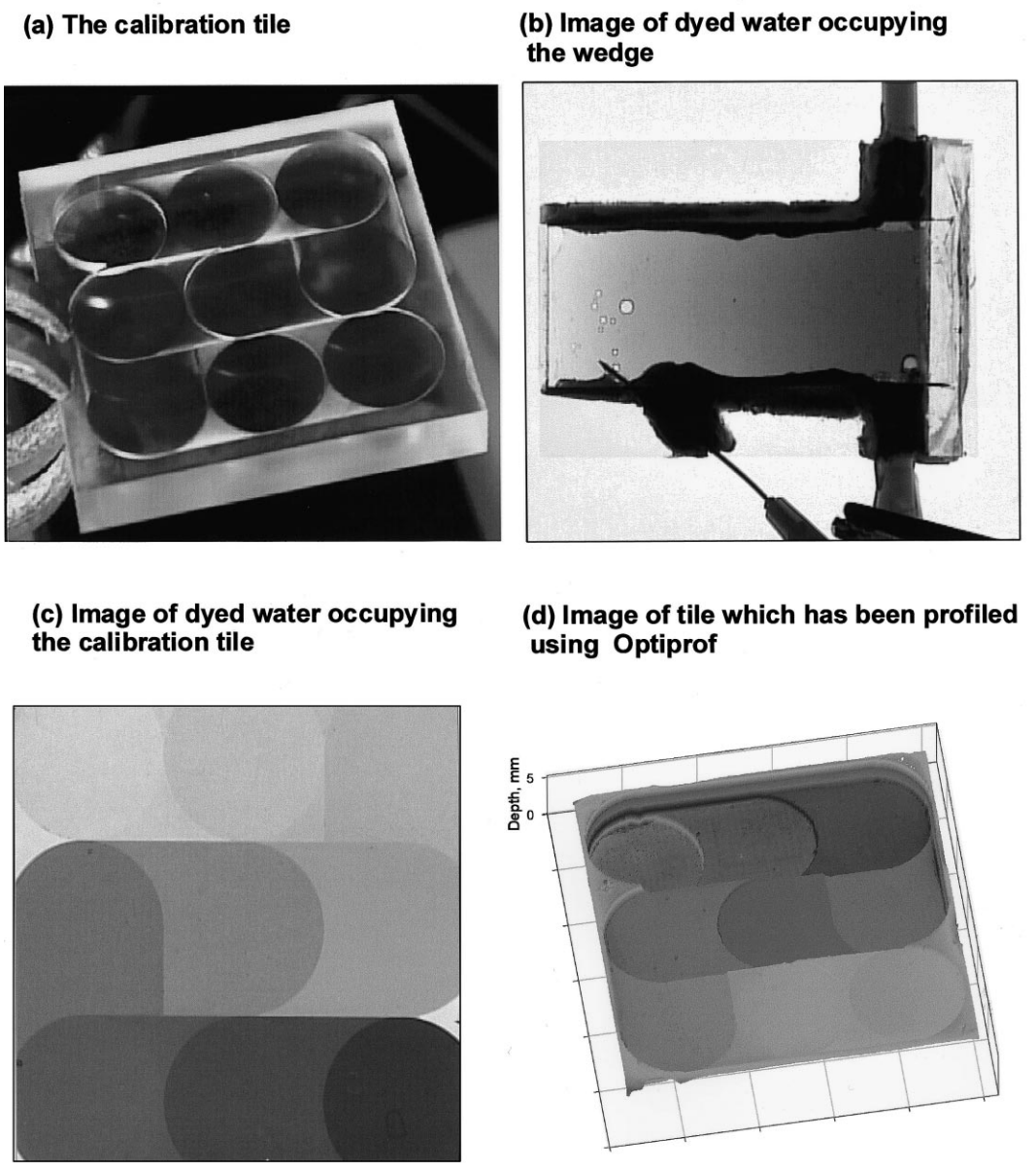

Fig. 5. Calibration devices. (a) The polycarbonate tile. (b) Image of dyed water occupying the wedge. (c) Image of dyed water occupying the calibration tile. (d) Profile of tile using OptiProf™.

I_o is the intensity of the incident light, K is a material-dependent property describing the efficiency with which a material adsorbs light, c is the concentration of the material, and T is the thickness of the material through which the light has passed.

Assume that we have a source of plane incoherent light of constant intensity and a camera, and we place between them first a polycarbonate housing containing dyed water with concentration of dye c_d and material extinction coefficient of the dye K_d. Subsequently, we place the same housing between the light source and the camera, but this time with the housing containing distilled water

(i.e. dyed water with material extinction coefficient K_d, but $c_d \rightarrow 0$). Let the thickness of fluid in each case be T and the total thickness of the polycarbonate housing be T_h, and let the material extinction property of the polycarbonate be $K_h c_h$. We can rewrite Eq. 1 for each of these scenarios:

$$I_{dye} = (I_o e^{-K_h c_h T_h}) \cdot (e^{-K_d c_d T}) \quad (2)$$

$$I_{water} = (I_o e^{-K_h c_h T_h}) \quad (3)$$

Since for water $c_d \rightarrow 0$, the second term in Eq. 3 becomes unity. If we take the ratio of Eq. 2 and Eq. 3 we get:

$$\frac{I_{dye}}{I_{water}} = e^{-K_d c_d T} \quad (4)$$

Knowledge of K_d and c_d would allow the thickness of dye T to be obtained from the intensities of light measured. While we know c_d for each fluid, K_d is unknown, hence we experimentally calibrate the intensity ratio I_{dye}/I_{water} as a function of fluid thickness T. This process provides the value of K_d for the dye. Once known, the thickness of dye T above a rough surface can be calculated for the measured light intensities and the values of K_d and c_d, thus:

$$T = \frac{\ln(I_{water}) - \ln(I_{dye})}{K_d c_d} \quad (5)$$

2.4. Fluid calibration

Here, more robust methodologies for calibrating the fluids used in the imaging process are described than the few previous attempts at fluid calibration [19,20].

Calibration was carried out on the fluids to be used in the imaging using two devices with accurately known fluid thicknesses; (i) a polycarbonate tile with nine wells of different depths, and (ii) a wedge-shaped vial made from silica glass. Calibration was carried out for distilled water and one known concentration of dyed water (1 g/l Dylon® Black), where the concentration had been chosen in a previous pilot study as that able to give the greatest range of intensities over the likely range of fracture apertures in our rocks (0–4 mm). A large amount of this dye was made to provide a stock of dye at the same concentration for subsequent work. A trace amount of formaldehyde was added to the dye to ensure that organic matter would not grow in the stock dye solution, and the stock was kept in a cool (20°C), totally dark cupboard when not in use to avoid bleaching of the dye. The stock solution was always shaken before to ensure that any settling and dye stratification that occurred while the dye was in store was removed.

The tile was constructed from a plate of polycarbonate, 9.5 mm thick (Fig. 5a). Nine wells were cut into the polycarbonate tile by a computer-controlled milling machine. The tile was then polished. The wells range from 0.25 ± 0.01 mm to 4.00 ± 0.01 mm depth, and were measured by laser interferometry.

The wedge was constructed from silica glass held together with epoxy, and incorporates tubes and hypodermic needles to facilitate its bubble-free filling (Fig. 5b). The plates of glass from which the wedge was constructed were assumed to be perfectly flat, such that the aperture of the wedge would vary linearly from its thin end (0.00 mm) to its thick end (4.30 ± 0.02 mm).

Each pocket of the tile was filled with each of the fluids, and a flat transparent cover plate was placed on top to seal the fluid in place during imaging. The presence of the top plate also removes the extra thickness of fluid that would have otherwise occurred due to the fluid meniscus. The filling and sealing was carried out under the fluid in question to avoid air bubbles. Some flakes of detergent were added into the fluid to prevent gas bubbles from forming. The tile was then imaged multiple times in the DOI set-up, producing eight-bit greyscale image intensities varying from 0 to 255 (Fig. 5c). The mean (stacked) image was calculated pixel by pixel to remove possible dynamic fluctuations in the incident light intensity or in the sampled video stream. The incident light was also imaged multiple times without the tile present in the form of eight-bit greyscale images. Again the average value was calculated pixel by pixel to remove dynamic fluctuations. This image contains information about possible spatial varia-

tions in the incident light, and is called a clearfield. The clearfield was then used to correct the average image of the tile to ensure that any spatial variations in incident light intensity were removed from the image. This process is called clearfield equalisation, and was carried out in SigmaScan Pro® image analysis software. The corrected image for the dyed water was divided pixel by pixel by that of the undyed water to remove the effect of the polycarbonate composing the tile and its cover plate, according to the process described by Eqs. 2–4. The resulting image represents the ratio of the intensities recorded when the calibration tile is full of dyed water and undyed water, and is solely dependent upon the fluid thickness if the type and concentration of the dye remain constant [19]. This image was analysed in SigmaScan Pro® to obtain the number of pixels present in each well for each intensity value, 0–255 (Fig. 6a). Gaussian curves were fitted to these data to obtain the mean intensity value and the standard deviation in intensity for each well. A calibration curve was then constructed of intensity as a function of fluid thickness from the data for all nine wells including error bars representing the standard deviations of intensity and thickness (Fig. 6b). The tile calibration data are given in Table 1.

A similar process was carried out for the wedge filled with both dyed and undyed water, and again converting to an eight-bit greyscale and using multiple images and clearfield equalisation. As the wedge provides a continuous variation of thicknesses and dye intensities, it was possible to obtain 440 data point pairs of intensity/thickness values but without information on the standard deviation of the intensity. Instead, this can be judged from the scatter in the large number of points from the wedge-derived data. The data from the wedge are also included in the calibration curve (Fig. 6b). It is clear that the tile calibration and the wedge calibration are in close agreement, and the scatter in the wedge data is similar to the standard deviation of the intensity from the tile-derived data. Furthermore, the wedge-derived data show that the calibration is uniform between the tile-derived data points. Note that this calibration curve is linear on the log–lin scales used in this diagram. The calibration curve therefore conforms to the Lambert–Beer law as expected, and we can derive a value for K_d of the dye, $K_d = 282.7$ m^2/kg. A function fitted to the tile-derived calibration data provides us with a conversion from intensity ratio to dye thickness that allows each pixel of the fracture intensity ratio map to be converted to a thickness of dye below the fluid surface. As the fluid surface is flat, we can therefore derive a measurement of the surface height at each pixel location.

2.5. Fracture surface imaging

It is now possible to image the individual fracture surfaces when covered with the dyed and undyed water. These images will then be calibrated using the data from the procedure described in the previous section to provide a map of the fluid thickness above the rough surface topography. Subsequently, the resulting data can be

Table 1
Tile calibration data

Well	Mean intensity ratio (eight-bit greyscale)	S.D. intensity data	Depth (mm)	S.D. depth data
A	235.62	3.750	0.91	0.025
B	220.04	3.368	0.42	0.068
C	207.56	3.164	0.69	0.083
D	195.24	3.522	0.91	0.022
E	169.25	3.049	1.50	0.105
F	146.01	3.112	1.96	0.010
G	124.51	2.948	2.53	0.013
H	104.98	2.949	3.01	0.027
I	81.450	2.807	3.91	0.014

S.D. = standard derivation

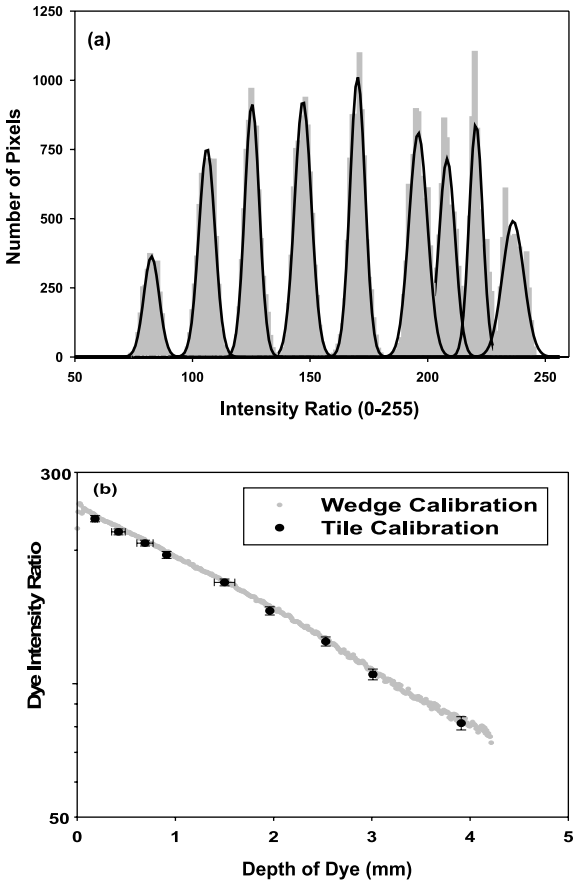

Fig. 6. The process of calibration. (a) The number of pixels in each well as a function of the ratio of the intensity with dyed water to that with undyed water (0–255, eight bits). (b) The calibration curve for both the tile-derived and the wedge-derived data.

transformed simply to provide a fully determined topography for each surface, and data from each of two surfaces can be combined to provide an aperture map of the fracture for the scenario where the surfaces touch at a single point or any greater mean aperture.

There are several technical difficulties to overcome in the imaging process in order that fracture surface roughnesses are profiled accurately. The technical difficulties are:

1. Each of the fractures must be filled with dyed and undyed water up to exactly the same arbitrary level; a level sufficient to cover the highest asperity.
2. Once each fracture has been imaged with the undyed fluid, the fluid must be replaced completely with the dyed fluid while maintaining the position of the HFPM relative to the camera to within one pixel in the x- or y-directions.
3. The light source and video stream (camera, cables, graphics capture card) has dynamic noise which leads to variations in brightness of the imaged intensities. This variation is small, but noticeable, and will contribute to errors in the final calculated heights of the surface.
4. There is a slight but noticeable low contrast broken stripe effect on an image of a uniform field, which varies with camera lens aperture. This may be a result of the non-uniform sensitivity of the camera CCD across its surface from pixel to pixel, but it is more likely to result from static distortion associated with video capture using the Matrox® video card.
5. The light source is slightly non-uniform across the imaged field.
6. It is almost impossible to ensure that small specks of dust and small bubbles are removed from the fluids when placed on the surfaces of the HFPM. These bubbles and dust specks are mobile if the fluid is perturbed.
7. There may be small opaque particles trapped in the HFPM.

All of these technical difficulties have been overcome. The solution to most of them has been achieved by the development of software written by the authors that (i) calibrates the imaging system, (ii) controls the capture of images, (iii) makes appropriate corrections, and (iv) calculates the final measured topography of the surface. This software is written in C++ and is called OptiProf™. The solution to each technical problem is discussed in turn below.

2.5.1. Fluid level control

The level of fluids in the fracture is obtained by etching onto opposite walls surrounding the fracture a horizontal datum line. Dyed or undyed

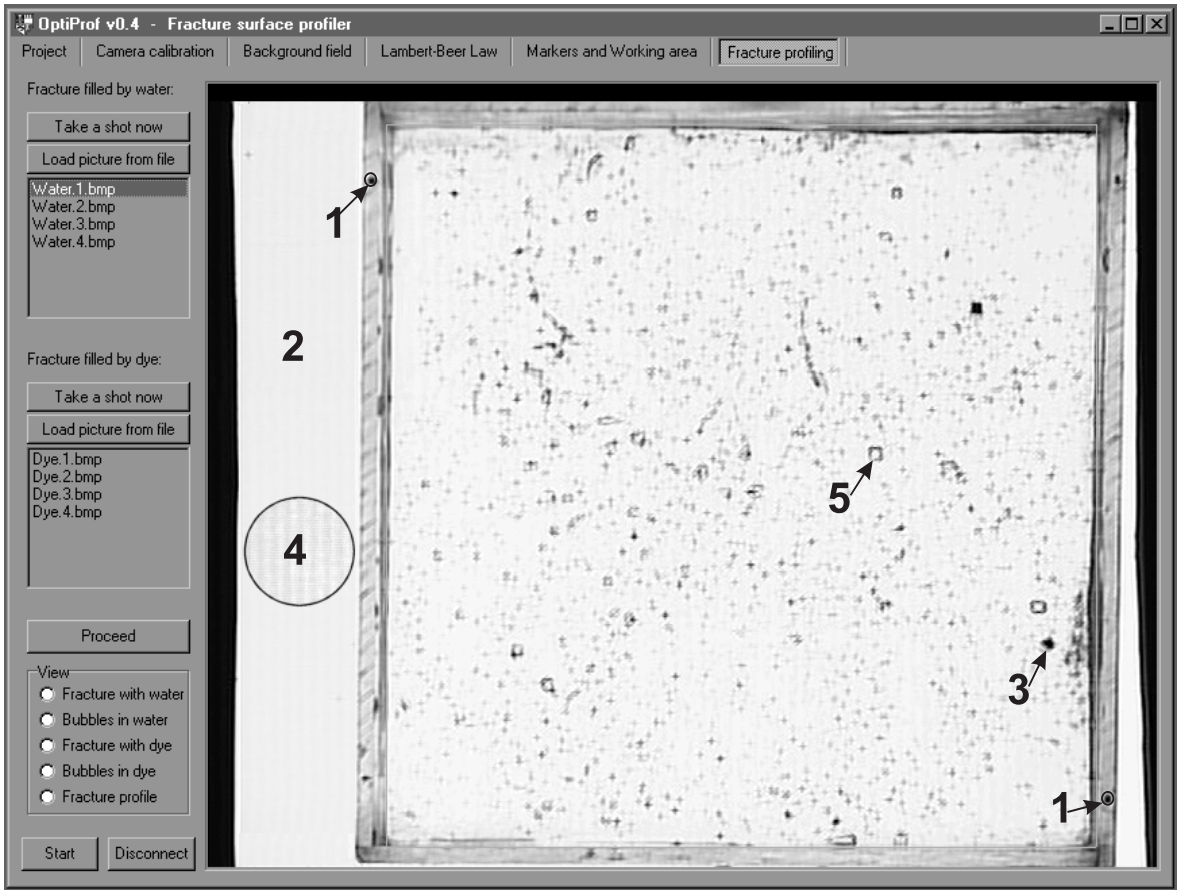

Fig. 7. An image of the HFPM during measurement by the software showing the different technical difficulties encountered. (1) Usage of location marks on walls to lock HFPM in position during imaging. (2) Dynamic noise across whole image. (3) Particles in the HFPMs. (4) Static distortions giving regular structure in video signal. (5) Bubbles and dust in fluids.

water is then placed into the fracture up to the mark closest to the user while the two marks are aligned by eye to avoid parallax errors.

2.5.2. *Lateral alignment*

Lateral alignment is assured by setting four fixed reference points defined by the small symbol (○) over point marks that are etched into the top of the walls surrounding the fracture (label 1 on Fig. 7). The fracture is filled with the undyed water and placed under the camera. The software images the fracture continuously, during which time each of the reference points are activated, moved carefully, pixel by pixel by mouse and keyboard arrows, to be exactly over the points etched into the walls of the fracture, and locked in place on the monitor screen. The HFPM containing the undyed water can then be imaged for the measurement. The HFPM can be removed, emptied, cleaned, and filled with the dyed water. It can then be placed in exactly the same position under the camera using continuous imaging of the HFPM and aligning the HFPM such that the points etched on its wall tops coincide with the fixed reference points on the monitor screen. The reference points are shown in Fig. 7 aligned with the etched marks on the HFPM walls.

2.5.3. *Dynamic noise in the imaged light intensity*

Dynamic noise in the light source and video stream is removed by making multiple images of the HFPM with each fluid in place, and averaging

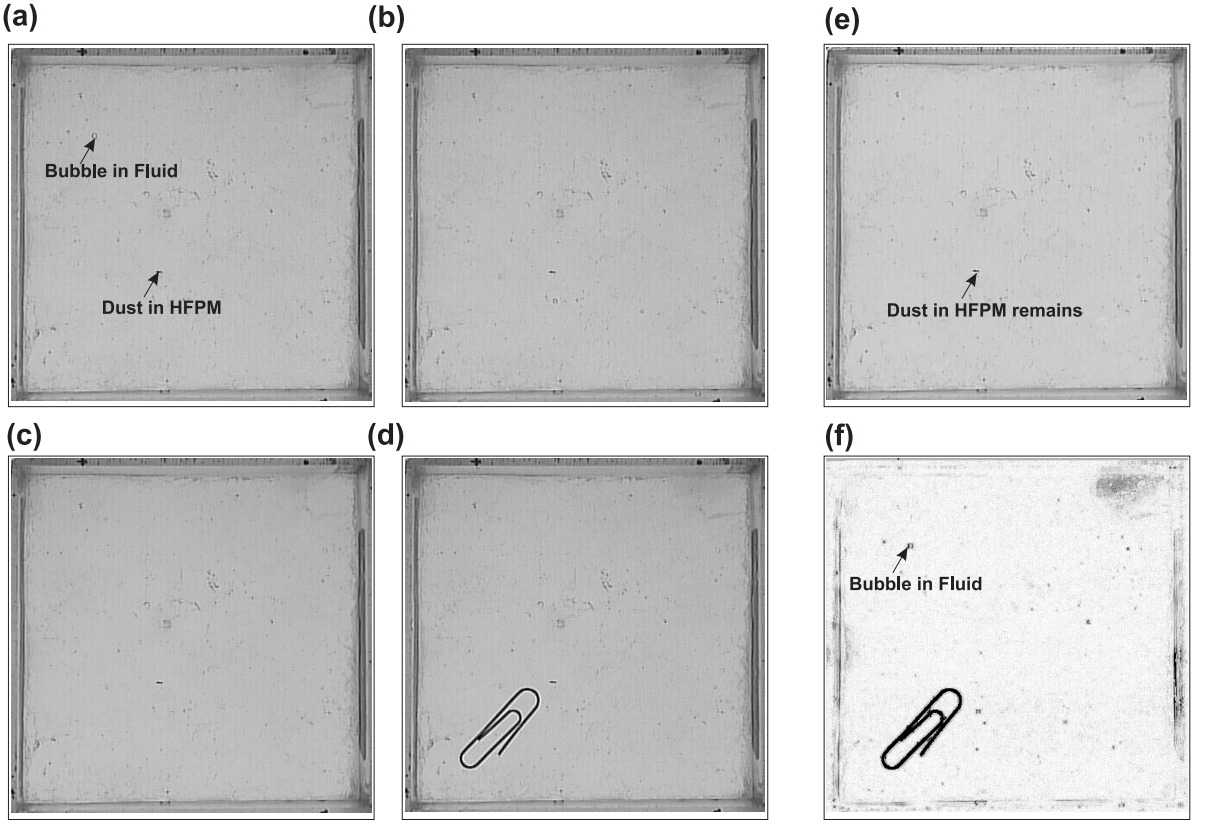

Fig. 8. The efficacy of artifact, bubble and dust particle removal by OptiProf™ software. (a–d) Four original images taken by the OptiProf™ software, with stirring between each one and a paperclip added to one of them. (e) The processed final image. (f) The resulting artifact map.

the result pixel by pixel. 20–50 images taken every second were found to be sufficient to remove the dynamic noise.

2.5.4. Static distortions in the video signal

The variation in the sensitivity of the CCD between each pixel on its surface (label 4 in Fig. 7) was removed by calibrating each pixel of the CCD individually. Light flux intensity was varied with the lens aperture. This procedure takes only 10 min. The procedure involves the imaging of the light source multiple times at each aperture. The images for each aperture are averaged to remove dynamic noise, then each pixel is calibrated to reduce or enhance its sensitivity to the mean value for the CCD array. An attenuator (16 dB) was connected to the Matrox® video capture board to further reduce static noise. Fig. 7 shows an area of the image that has been contrast enhanced to show the structure of the original field, without the use of an attenuator and uncalibrated for CCD sensitivity. This is completely removed by the software pixel calibration process.

2.5.5. Non-uniformity of the light source

The images were corrected for the slight non-uniformity in the light source by doing a clearfield equalisation. The clearfield was obtained by taking multiple images of the light source, and averaging them to remove dynamic noise. Each of the averaged intensity images from the measurements on the undyed and dyed water were then subjected to a clearfield equalisation using the clearfield image, during which process any variations due to changes in the incident light source intensity are removed.

2.5.6. Bubbles and dust in the fluids

Particles and bubbles in the fluids (label 5, Fig. 7) are mobile if the fluid is perturbed. The presence of bubbles and dust can be recognised as an artefact by the software in the following way. The dyed or undyed water is imaged three to five times. Each of these images were composed of multiple frames to avoid the dynamic noise. The fluid is stirred carefully between taking each image, which moves bubbles and dust in the fluid to another location. The software compares the images and recognises characteristics which move. These are then removed from the relevant images prior to averaging. The final positions of the bubbles and dust are plotted on an image map of artefacts that the software records, and which may be viewed during processing. The efficacy of this procedure is demonstrated clearly by Fig. 8. This figure shows an image of a HFPM containing undyed water. Four images were taken (Fig. 8a–d), stirring carefully between each image, and for the final image a paperclip was added to the HFPM. As a result of the above procedure, the image of the paperclip has been removed effectively from the final averaged image (Fig. 8e), and its shape and position can be seen clearly in the artefact map (Fig. 8f). The other smaller perturbations in the artefact map are dust particles and bubbles.

2.5.7. Opaque particles in the HFPM

These are immobile but small and uncommon (label 3 in Fig. 7). They are present in all images and not removed by any of the previously mentioned procedures. They are extremely obvious in the final image as thin low intensity spikes, and are recognised by the software and removed, with the affected pixel being reduced to the weighted mean of the surrounding eight pixels.

The acquisition software processing is semi-automatic and arranged in a logical procedure.

3. Determinations on test pieces and rock fractures

3.1. Test pieces

The effectiveness of the technique was first tested using the calibration tile. In this procedure the tile was re-imaged with dyed and undyed water assuming it to take the place of the HFPM. The software was allowed to carry out its full range of calculations, and the result is shown in Fig. 5d. The mean well depths and standard deviations in well depth have been calculated from the resulting data and compared with the same values initially measured on the tile by laser interferometry. It is clear from this figure that the depths of the tile wells are well reproduced by the new technique, with a standard error in the mean of approximately ± 0.04 mm (± 0.02 mm–± 0.01 mm depending on well depth).

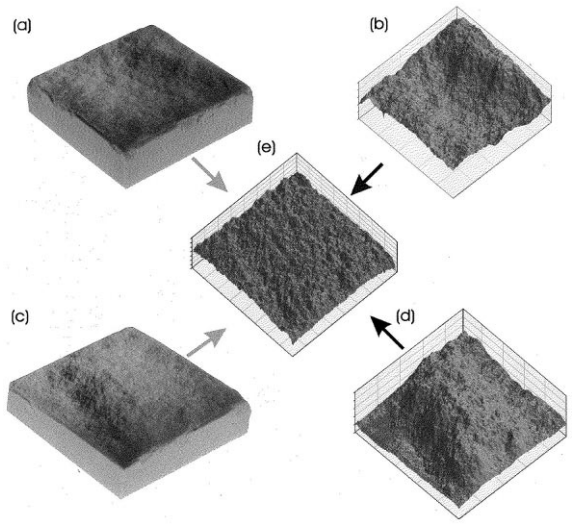

Fig. 9. Fracture surface profile for sample A. (a) Image of fracture surface 1. (b) Profile of fracture surface 1. (c) Image of fracture surface 2. (d) Profile of fracture surface 2. Black arrows show derivation of fracture aperture map (e) from profiling data and grey arrows show relationship of aperture map to real rock fractures.

3.2. Rock fractures

Core analysis data are provided for the rock samples used in this study (Table 2). Core plugs (1.5 inch diameter) were taken from the samples and subjected to Hassler sleeve gas permeametry and helium porosimetry and the offcuts were used in the determination of mercury injection porosity. Sample A is the Clashach sandstone from NE Scotland; a medium grained, texturally and min-

Table 2
Petrographic and petrophysical data for samples

Sample code	Rock type	Sample location	Grain size	Hgϕ	S_{wi} (%)	Heϕ (%)	K_L (mD)	Point count data (%)					
								Q	K	P	A	R	M
A	sandstone	NE Scotland	medium	8.40	73.4	8.90	21.2	77.5	12.5	0.00	0.00	9.50	0.50
B	syenite	Sweden	coarse	1.20	94.5	0.20	0.02	5.50	70.0	7.00	11.6	0	5.90
C	granite	S. Norway	coarse	0.50	99.2	4.45	1.01	21.2	44.3	29.5	2.70	0	2.30

Hgϕ, mercury injection porosity; S_{wi}, irreducible water saturation derived from mercury porosimetry; Heϕ, helium porosity; K_L, Klinkenberg-corrected permeability; Q, quartz; K, alkali feldspar; P, plagioclase; A, amphibole; R, rock fragments; M, mica.

eralogically mature aeolinite. Samples B (Swedish syenite) and C (Norwegian granite) are coarsely crystalline igneous rocks, the surfaces of which have anisotropic roughness defined by laths of dominantly K-feldspar. Sample A has considerably higher porosity and permeability values and the lowest irreducible water saturation, S_{wi} than samples B and C (Table 2).

The rock fracture surfaces in these rocks have been imaged with the new technique, and these are summarised in Table 3. The samples were trimmed and fractured in a controlled fashion in the laboratory. HFPMs were constructed from each fracture face of each block, and were submitted to the new technique. The same batch of dye, of fixed concentration was used in all tests, and this dye was calibrated using the methods described above. Figs. 9 and 10 show photographs of fracture surfaces of samples A and B (a, c), the measured surface topographies (b, d), and the aperture calculated when opposite surfaces touch at a single point (e).

In each case the profiles are very accurate representations of the fracture surfaces. There are however some spikes in the profiles, which may be artefacts in the HFPMs which were not removed by the image processing techniques described. These should have no bearing upon synthetic modelling of these surfaces [25].

Previous studies show that the hydraulic aperture is proportional to a complex average of the aperture distribution [26]. In fact, the geometric mean of the fracture aperture has been popularly used to estimate the hydraulic aperture [27–29]. The hydraulic aperture calculated using geometric mean becomes zero if any touching point exists, which is reasonable for a 2D model where any touching point completely closes the fracture channel. The situation is however more complex for real 3D fractures. A new approach is used in this study to derive hydraulic aperture, which we call the dual mean, and is a combination of geometric and arithmetic means (Table 3). Single touching points affect the fluid flow locally and do not change the overall hydraulic aperture dramatically. We assume that flow streamlines are straight and parallel to the pressure gradient and that we can find the hydraulic aperture (determined along each of the streamlines as a geometric mean aperture). As the overall fracture con-

Table 3
Rock fractures tested with the new method

Sample code	Rock type	σ_l (mm)	σ_u (mm)	$\langle z\rangle_a$ (mm)	$\langle z\rangle_h^a$ (mm)	$\langle z\rangle_g^a$ (mm)	$\langle z\rangle_{dx}$ (mm)	$\langle z\rangle_{dy}$ (mm)
A	sandstone	2.32	2.08	2.03	0	0	1.75	1.80
B	syenite	1.65	1.56	1.95	0	0	1.75	1.79
C	granite	1.62	1.51	2.50	0	0	2.33	2.27

σ_l, standard deviation of surface heights for lower fracture surface; σu, standard deviation of surface heights for upper fracture surface; $\langle z\rangle a$, arithmetic mean of fracture aperture; $\langle z\rangle h$, harmonic mean of fracture aperture; $\langle z\rangle g$, geometric mean of fracture aperture; $\langle z\rangle dx$, dual mean of fracture aperture in x-direction; $\langle z\rangle dy$, dual mean of fracture aperture in y-direction.
[a]Harmonic and geometric means of the fracture are 0 because at least one touching point exists, where the aperture is 0.

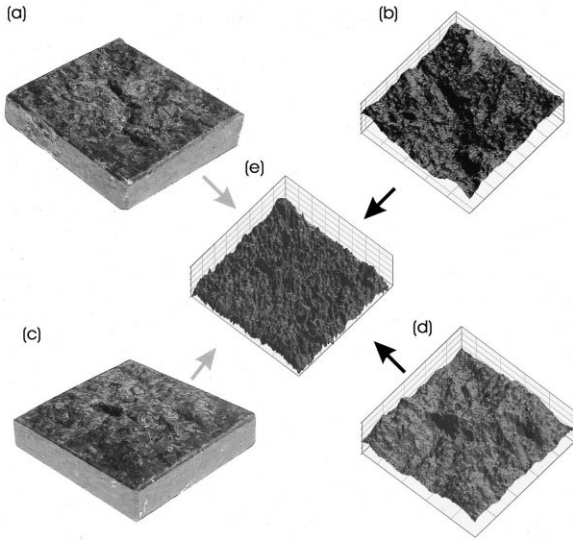

Fig. 10. Fracture surface profile for sample B. (a) Image of fracture surface 1. (b) Profile of fracture surface 1. (c) Image of fracture surface 2. (d) Profile of fracture surface 2. Black arrows show derivation of fracture aperture map (e) from profiling data and grey arrows show relationship of aperture map to real rock fractures.

ductivity is a sum of the conductivities along each streamline, the overall hydraulic aperture of the fracture can be approximated by the arithmetic mean of the individual hydraulic apertures along the streamlines. Hence the dual mean of a 3D aperture is the geometric mean along each streamline (i.e. to first approximation, in the direction of flow) arithmetically averaged perpendicular to flow. Therefore, the dual mean aperture in general has different values for each flow direction through the fracture and is anisotropic.

4. Resolution of the method

The lateral resolution of the method depends upon (i) the fidelity of the HFPM, (ii) the number of pixels in the image, and (iii) the imaged area. We know from the SEM tests on the HFPMs that the fidelity of fracture reproduction is better than 1 μm. In our work we used a camera with a pixel array of 640×480 (307 200 pixels). When the camera was used in its widest zoom mode, 100×100 mm of the fracture surface was imaged with a resolution of 200 μm. When the camera was used in its highest zoom mode, 10×7.5 mm of the fracture surface was imaged with a resolution of 15.6 μm. Cameras are now available with 3.3 million pixels, which, if used, would give a lateral resolution of 50 μm for an image area of 100×75 mm, and 5 μm for an image area of 10×7.5 mm.

The vertical resolution is similar to the above but better vertical resolution may be achieved through increasing the greyscale depth from eight bits to 24 bits. Nevertheless, this technique has greater lateral resolution than the other techniques for obtaining fracture surface roughness. Furthermore, it is inexpensive, non-destructive and provides continuous coverage of the surface topography.

5. Conclusions

A new, fast and inexpensive optical method has been developed that allows the numerical determination of the surface topography and aperture of rough fractures in rocks. The method relies on the calibration of a dyed fluid, which obeys the Lambert–Beer law, and has been successfully tested upon HFPMs of real rock fractures. This method involves new developments that make existing concepts (i.e. spectrophotometric analysis of epoxy casts) into a useful method for determining rough fracture apertures.

Firstly, advances in HFPM preparation result in fidelity of reproduction at the submillimetre scale ($<+1$ μm). There are improvements in hardware image capture from previous attempts [1,19,23,24] using high quality digital cameras and video streams. This method has a high lateral resolution, which was 15 μm for our camera/imaging set-up but can be better than this if higher resolution cameras are used. It has a similar height resolution (15 μm) for our set-up, but again could be smaller if 16-bit or 24-bit imaging hardware is used. The method also benefits from improvements in firmware image capture, i.e. the capturing of images from the camera through to the final stored images. Advances in the multiple capture of images from the video stream have im-

proved the quality of the initial images as well as making advanced image analysis options possible on the captured image data; something that was not possible previously.

Robust methodologies have been developed for reliably calibrating the fluids used in the imaging process. This allows the Lambert–Beer law to be applied to the measured data to convert intensities ultimately into accurate surface heights. Although the Lambert–Beer law has been used previously, few studies report the calibration of the fluids used in the imaging process [19,20], which resulted in only arbitrarily scaled relative surface height measurements being possible [1,23].

In-house developed OptiProf™ software was used for the analysis of the image data to correct for and negate problems with the image capture process. Techniques that are newly implemented are (i) multiple imaging, (ii) clearfield equalisation, (iii) stacking, (iv) software keying, (v) bubble detection, (vi) static detection, (vii) individual pixel calibration, and (viii) precise filling. This software can be obtained free of charge from the authors at http://petrophysics.webhop.net/.

A full comparative analysis of the sources of error in the measurements, together with the scope for their reduction is presented. This is a necessary item in a study such as this, but is rarely carried out [17]. It is essential to allow the accuracy of the resulting profiling data to be judged. The lack of such an analysis in many of the previous papers may stem from a lack of confidence in some of the relatively primitive methods then being employed [1,23,24].

A new definition of mean aperture is used (the dual mean) which removes the difficulty of zero-calculated aperture for rock apertures that touch at a single point, but is physically reasonable.

Acknowledgements

This work was funded by the Natural Environmental Research Council of the UK, as part of the Micro-to-Macro Thematic Programme. *[AC]*

References

[1] S. Brown, A. Caprihan, R. Hardy, Experimental observation of fluid flow channels in a single fracture, J. Geophys. Res. 103 (1998) 5125–5132.
[2] P.E. Dijk, B. Berkowitz, P. Bendel, Investigation of flow in water-saturated rock fractures using nuclear magnetic resonance imaging (NMRI), Water Resour. Res. 35 (1999) 347–360.
[3] P.E. Dijk, B. Berkowitz, Three-dimensional flow measurements in rock fractures, Water Resour. Res. 35 (1999) 3955–3959.
[4] M. Lespinasse, J. Sausse, Quantification of fluid flow: hydro-mechanical behaviour of different natural rough fractures, J. Geochem. Explor. 69–70 (2000) 483–486.
[5] F. Plouraboue, P. Kurowski, J.-P. Hulin, S. Roux, J. Schmittbuhl, Aperture of rough cracks, Phys. Rev. E 51 (1995) 1675–1685.
[6] S.R. Brown, Fluid Flow through rock joints: The effect of surface roughness, J. Geophys. Res. 92 (1987) 1337–1347.
[7] P.W.J. Glover, K. Matsuki, R. Hikima, K. Hayashi, Synthetic rough fractures in rocks, J. Geophys. Res. 103 (1998) 9609–9620.
[8] P.W.J. Glover, K. Matsuki, R. Hikima, K. Hayashi, Fluid flow in synthetic rough fractures and application to the Hachimantai geothermal HDR test site, J. Geophys. Res. 103 (1998) 9621–9635.
[9] W.L. Power, T.E. Tullis, Euclidian and fractal models for the description of rock surface roughness, J. Geophys. Res. 96 (1991) 415–424.
[10] J. Schmittbuhl, F. Schmitt, C.H. Scholz, Scaling invariance of crack surfaces, J. Geophys. Res. 100 (1995) 5953–5973.
[11] R.W. Zimmerman, I.W. Yeo, Fluid flow in rock fractures: From the Navier–Stokes equations to the Cubic law, in: B. Faybishenko, P.A. Witherspoon, S.M. Benton (Eds.), Dynamics of Fluids in Fractured Rock, Geophys. Monogr. 122, AGU, 2000, pp. 213–224.
[12] S.R. Brown, H.W. Stockman, S.J. Reeves, Applicability of Reynolds equation for modelling fluid flow between rough surfaces, Geophys. Res. Lett. 22 (1995) 2537–2540.
[13] S.R. Brown, R.L. Kranz, B.P. Bonner, Correlation between the surfaces of natural rock joints, Geophys. Res. Lett. 13 (1986) 1430–1433.
[14] C.F. Voss, L.R. Shotwell, An investigation of the mechanical and hydraulic behaviour of tuff fractures under saturated conditions, in: High Level Radioactive Waste Management, Am. Nucl. Soc., La Grange Park, IL, 1990, pp. 825–834.
[15] M.W. Jessel, S.J.D. Cox, P. Schwarze, W.L Power, The anisotropy of surface roughness measured using a digital photogrammetric technique, in: M.S. Ameen (Ed.), Fractography: Fracture Topography as a Tool in Fracture Mechanics and Stress Analysis, Geol. Soc. London Spec. Publ. 92, 1995, pp. 27–37.

[16] N.H. Maerz, J.A. Franklin, C.P. Bennett, Joint roughness measurements using shadow profilometry, Int. J. Rock Mech. Min. Sci. Abstr. 27 (1990) 329–343.
[17] R.L. Detwiler, L. Russel, S.E. Pringle, E. Scott, R.J. Glass, Measurement of fracture aperture fields using transmitted light: An evaluation of measurement errors and their influence on simulations of flow and transport through a single fracture, Water Resour. Res. 35 (1999) 2605–2617.
[18] H. Amundsen, G. Wagner, U. Oxaal, P. Meakin, J. Feder, T. Jossang, Slow-two-phase flow in artificial fractures: Experiments and simulations, Water Resour. Res. 35 (1999) 2619–2626.
[19] P. Persoff, K. Pruess, Two-Phase flow visualization and relative permeability measurement in natural rough-walled rock fractures, Water Resour. Res. 31 (1995) 1175–1186.
[20] C.E. Renshaw, J.-S. Dadakis, S.R. Brown, Measuring fracture apertures: A comparison of methods, Geophys. Res. Lett. 27 (2000) 289–292.
[21] R.A. Johns, J.S. Steade, L.M. Castanier, P.V. Roberts, Non destructive measurements of fracture aperture in crystalline rocks using X-ray computed tomography, J. Geophys. Res. 98 (1993) 1889–1900.
[22] A.A. Keller, Single and Multiphase Flow and Transport in Fractured Porous Media, Ph.D. Dissertation, Stanford University, Stanford, CA, 1996.
[23] E. Hakami, E. Larsson, Aperture measurements and flow experiments on a single natural fracture, Int. J. Rock Mech. Min. Sci. Abstr. 33 (1996) 395–404.
[24] I.W. Yeo, M.H. De Freitas, R.W. Zimmerman, Effect of shear displacement on the aperture and permeability of a rock fracture, Int. J. Rock Mech. Min. Sci. Abstr. 35 (1998) 1051–1070.
[25] E. Isakov, S.R. Ogilvie, P.W.J. Glover, Modelling fluid flow through rough fractures in rocks II: Fracture analysis and synthetic fracture modelling, Earth Planet. Sci. Lett., submitted.
[26] A.P. Oron, B. Berkowitz, Flow in rock fractures: The local cubic law assumption reexamined, Water Resour. Res. 34 (1998) 2811–2825.
[27] S.R. Brown, A note on the description of surface roughness using fractal dimension, Geophys. Res. Lett. 14 (1987) 1095–1098.
[28] C.E. Renshaw, On the relationship between mechanical and hydraulic apertures in rough-walled fractures, J. Geophys. Res. 100 (1995) 24629–24636.
[29] M. Iwano, H.E. Einstein, Laboratory experiments on geometric and hydromechanical characteristics of three different fractures in granodiorite, in: T. Fuji (Ed.), Int. Congr. Rock Mech. Proc. 2, Tokyo, 1995.